# Practical loss tangent imaging with amplitude-modulated atomic force microscopy

Roger Proksch, Marta Kocun, Donna Hurley, Mario Viani, Aleks Labuda, Waiman Meinhold, and Jason Bemis

**Articles you may be interested in**

Bifurcation, chaos, and scan instability in dynamic atomic force microscopy
J. Appl. Phys. **119**, 125308 (2016); 10.1063/1.4944714

Hydrodynamic corrections to contact resonance atomic force microscopy measurements of viscoelastic loss tangenta)
Rev. Sci. Instrum. **84**, 073703 (2013); 10.1063/1.4812633

Power spectrum analysis with least-squares fitting: Amplitude bias and its elimination, with application to optical tweezers and atomic force microscope cantilevers
Rev. Sci. Instrum. **81**, 075103 (2010); 10.1063/1.3455217

Frequency noise in frequency modulation atomic force microscopy
Rev. Sci. Instrum. **80**, 043708 (2009); 10.1063/1.3120913

Atomic force microscopy spring constant determination in viscous liquids
Rev. Sci. Instrum. **80**, 035110 (2009); 10.1063/1.3100258

CrossMark
click for updates

# Practical loss tangent imaging with amplitude-modulated atomic force microscopy

Roger Proksch,[1,a] Marta Kocun,[1] Donna Hurley,[2] Mario Viani,[1] Aleks Labuda,[1] Waiman Meinhold,[1] and Jason Bemis[1]

[1]*Asylum Research, an Oxford Instruments Company, Santa Barbara, California 93117, USA*
[2]*Lark Scientific LLC, Boulder, Colorado 80302, USA*

Amplitude-modulated (AM) atomic force microscopy (AFM), also known as tapping or AC mode, is a proven, reliable, and gentle imaging method with widespread applications. Previously, the contrast in AM-AFM has been difficult to quantify. AFM loss tangent imaging is a recently introduced technique that recasts AM mode phase imaging into a single term $\tan \delta$ that includes both the dissipated and stored energy of the tip-sample interaction. It promises fast, versatile mapping of variations in near-surface viscoelastic properties. However, experiments to date have generally obtained values larger than expected for the viscoelastic loss tangent of materials. Here, we explore and discuss several practical considerations for AFM loss tangent imaging experiments. A frequent limitation to tapping in air is Brownian (thermal) motion of the cantilever. This fundamental noise source limits the accuracy of loss tangent estimation to approximately $0.01 < \tan \delta < 5$ in air. In addition, surface effects including squeeze film damping, adhesion, and plastic deformation can contribute in a manner consistent with experimentally observed overestimations. For squeeze film damping, we demonstrate a calibration technique that removes this effect at every pixel. Finally, temperature-dependent imaging in a two-component polymeric film demonstrates that this technique can identify temperature-dependent phase transitions, even in the presence of such non-ideal interactions. These results help understand the limits and opportunities not only of this particular technique but also of AM mode with phase imaging in general. © 2016 AIP Publishing LLC. [http://dx.doi.org/10.1063/1.4944879]

## I. INTRODUCTION

Gentle, high-resolution characterization with sensitivity to mechanical properties has been an ongoing goal of atomic force microscopy (AFM) since its advent.[1,2] The ability to characterize both viscoelastic and elastic responses on the nanoscale is increasingly important in successful development of advanced materials. To achieve this goal, various AFM techniques have been developed over the years. Initially, these techniques could typically provide only qualitative information, with image contrast related to various mechanical properties. However, recent years have seen great strides towards the ultimate goal of quantitative nanomechanical imaging.

One of the most popular AFM imaging modes is "tapping mode,"[3] also known as intermittent contact (AC) or amplitude-modulated (AM) mode. The term "tapping" was coined by Finlan,[4] who was among the first[2,5] to describe the mode. Independent discoveries by Gleyzes[6] on bistability and other effects laid the first foundations of theoretical understanding, and commercialization followed shortly thereafter.[7,8] In this mode, the cantilever is driven at a frequency close to or at that of its lowest resonance mode. The amplitude and the phase of cantilever oscillations are detected with a lock-in amplifier. On approaching the surface, tip-surface interactions damp the cantilever amplitude. The amplitude can thus be used as a feedback signal for topographic imaging. Significant advantages of AM mode include strongly reduced tip and surface damage, which allows imaging of much softer samples compared to contact mode.

Another advantage of AM mode is that it allows detection of the phase of the cantilever response, referred to as "phase imaging." Phase imaging was a source of much excitement beginning in the late 1990s, when the first phase images of a wood pulp sample[9] revealed microstructure not visible in the topography image. Since then, it has become a central technique in AFM materials imaging. It is most notably used in polymer characterization, where the phase channel is often capable of resolving fine structural details and discriminating between various material components.[10–16]

Many approaches have been developed to interpret the phase response in terms of the mechanical[17–22] and chemical[23] properties of the sample surface. A key realization was that phase contrast in AM mode operation does not depend on a sample's elastic properties, if the tip-sample interaction is purely elastic.[24] Soon afterward, an analytical expression was derived to relate the phase in AM mode to the tip-sample dissipation in the case of inelastic interactions.[25] Since those pioneering works, progress has been made in quantifying energy dissipation and storage between the tip and the sample,[26–28] with the goal of linking it to specific material properties. The phase response depends not only on how the material stores elastic energy and dissipates viscous energy but also on many other dissipative forces. In addition, other factors that influence the phase response must be considered, including tip radius, and cantilever vibrational and feedback parameters.

a)Author to whom correspondence should be addressed. Electronic mail: Roger.Proksch@oxinst.com

**119**, 134901-1

Recently, phase contrast has been recast in terms of loss tangent concepts.[29] As with other mechanical measurements, the indentation into a surface results in both elastic and inelastic dissipative processes. In the limit where the tip-surface interaction is a linear viscoelastic process,[30] the ratio of the dissipative and elastic contributions is described by the loss tangent. By combining the amplitude and phase signals of AM mode, AFM loss tangent imaging offers the potential for nanomechanical property imaging with high spatial resolution and fast imaging rates.[31] However, the surface-sensitive nature of AM mode—a feature that results in its high resolution and reduced surface damage—complicates this simple interpretation.

In the following, we explore several practical considerations for AFM loss tangent imaging experiments. We discuss random and systematic errors and examine their effect on measurement capabilities. This analysis also allows a quantitative exploration of how sources of dissipation such as the surrounding air environment, absorbed water on the sample and tip, and sample plasticity can lead to *over*estimations in the dissipated energy. Ubiquitous attractive interactions, both long-ranged and adhesive, can lead to *under*estimations in the stored energy. These real-world complications all lead to overestimation of AM mode loss tangent values. The results provide insight into AFM loss tangent imaging as an experimental technique and aid its progress towards becoming a more accurate tool for quantitative nanomechanical imaging. In addition, while its interpretation in terms of the loss tangent is new, AM mode phase imaging is a venerable topic, having been practiced for more than two decades.[9] The insight provided by the analysis below also helps explain some of the trends and observations in phase imaging over the past twenty years, specifically the plethora of results on polymeric materials and the dearth on metals, ceramics, and glasses.

## II. PRINCIPLES OF AFM LOSS TANGENT IMAGING

The viscoelastic loss tangent[30] $\tan\delta$ of a material is a dimensionless parameter that measures the ratio of energy dissipated to energy stored in one cycle of a periodic deformation and is ubiquitous in the polymer literature.[32–34] This is similar to other dimensionless approaches to characterize loss and storage in materials such as the coefficient of restitution.[35] In terms of a material's mechanical properties, the loss tangent is defined as $\tan\delta = G''/G'$, where $G''$ is the shear loss modulus, and $G'$ is the shear storage modulus. If the material behaves like a linear viscoelastic material during the indentation cycle, the loss tangent is independent of the tip-sample contact area.[36–38] The concept of the loss tangent considers elastic energy and viscous dissipation jointly instead of treating them independently as energy storage (the virial) and dissipation. This approach is attractive for AFM experiments, where the two quantities are inextricably linked: a tip indenting a surface will both store elastic energy and dissipate viscous energy, and both the stored and dissipated energy will increase as the tip indents further into a surface.

In AM mode, the amplitude of the cantilever's first resonant mode is used to maintain the tip-sample distance. At the same time, the phase of the first mode will vary in response to the tip-sample interaction. This phase reflects

both dissipative[25] and conservative[28] interactions. The AFM loss tangent $\tan\delta$ of the tip-sample interaction is related to the measured cantilever amplitude $V$ (or equivalently, $A$) and phase $\phi$ of the first resonant mode by[29]

$$\tan\delta = \frac{\langle F_{ts} \cdot \dot{z}\rangle}{\omega\langle F_{ts} \cdot z\rangle} = \frac{\dfrac{\omega}{\omega_{\text{free}}}\dfrac{V}{V_{\text{free}}} - \sin\phi}{Q\dfrac{V}{V_{\text{free}}}\left(1 - \dfrac{\omega^2}{\omega_{\text{free}}^2}\right) - \cos\phi}$$

$$= \frac{\Omega\alpha - \sin\phi}{Q\alpha(1 - \Omega^2) - \cos\phi}. \tag{1}$$

In this expression, $F_{ts}$ is the tip-sample interaction force, $z$ is the tip motion, $\dot{z}$ is the tip velocity, $\omega$ is the angular frequency at which the cantilever is driven, $Q$ is the quality factor of the resonance, $V$ is the cantilever amplitude and the brackets $\langle\rangle$ represent a time average. The parameter $V_{\text{free}}$ is the "free" resonant amplitude of the first mode, measured at a reference position. Note that because the amplitudes appear as ratios in Eq. (1), they can be either calibrated or uncalibrated in terms of optical detector sensitivity. In the final expression in (1), we have defined the ratios $\Omega \equiv \omega/\omega_{\text{free}}$ and $\alpha \equiv A/A_{\text{free}} = V/V_{\text{free}}$. Equation (1) differs by a factor of $-1$ from an earlier expression[29] because we have adopted the convention that the virial $\langle F_{ts} \cdot z\rangle$ is positive when the net forces between the tip and the sample are repulsive. The convention that $\langle F_{ts} \cdot z\rangle > 0$ results in $\tan\delta > 0$, consistent with a common convention in the polymer literature. This corresponds to an imaging condition commonly referred to as "repulsive mode" and represents the situation where forces between the tip and the sample are dominated by viscoelastic contact forces rather than long range electrostatic, van der Waals, or other attractive forces. If we operate in AM mode at the free resonance frequency (i.e., $\Omega = 1$), the AFM loss tangent expression can be simplified to

$$\tan\delta \approx \frac{\sin\phi - \alpha}{\cos\phi}. \tag{2}$$

It is important to note that both Eqs. (1) and (2) involve the cantilever amplitude only through the ratio $\alpha$. Thus, the AFM loss tangent does not depend on precise measurements of the optical lever sensitivity, in contrast to techniques such as force-distance curves. This has the potential to significantly reduce a source of systematic error.[39] In the above expressions, we deliberately used $V$ (units of volts) to signify amplitude instead of $A$ (units of meters) to explicitly indicate that a calibrated value of the optical lever sensitivity is not needed.

The following are some important implications of these equations, all three of which result in an overestimation of the sample loss tangent.

(1) In addition to contact repulsive viscoelastic forces, attractive (negative) interactions between the tip and the sample, averaged over an oscillation cycle, will make the elastic denominator $\langle F_{ts} \cdot z\rangle$ of Eqs. (1) and (2) smaller.

(2) Tip-sample damping with origins other than the sample loss modulus, for example, those originating from interactions with a water layer on either the tip or the sample, will increase the numerator in Eqs. (1) and (2).

(3) When the net forces on the cantilever are attractive, it implies a negative frequency shift, or equivalently, a positive phase shift $\phi > 90°$. In this case, Eqs. (1) and (2) will actually return negative values for the loss tangent. Other sources of dissipation discussed below, such as squeeze film damping and plasticity, are additive. This increases the numerator in Eqs. (1) or (2), resulting in an overestimation of the loss tangent.

These implications point out an important limitation of AFM loss tangent imaging. Equations (1) and (2) should be thought of as the combined loss tangent of the cantilever *and* the tip-sample interaction. Depending on instrumental and sample properties, this may or may not correspond to the loss tangent $\tan \delta = G''/G'$ originating from the linear viscoelastic behavior of the sample mechanics. In addition to the desired dissipative and elastic properties of the surface material, the measured AFM loss tangent includes contributions from other effects including changes in squeeze film damping, surface contamination, chemical adhesion, plastic deformation of the material, and perhaps even long-ranged electromagnetic interactions. In other words, we are measuring the ratio of the total conservative and dissipative responses of the cantilever as it interacts with the surface.

## III. LOSS TANGENT IMAGING EXPERIMENTS

AFM loss tangent imaging promises high-speed nanomechanical characterization with more reliable contrast than conventional phase imaging. To illustrate the potential of loss tangent imaging and to further explore the implications of the above discussion, we present experimental results for two different samples: a polymer blend and a metallic solder.

## A. Temperature-dependent imaging of polymers

In polymer research, the viscoelastic loss tangent is commonly used to identify phase transitions such as the glass transition or the melting transition. In the linear viscoelastic limit, the loss tangent is independent of geometric effects and can therefore be considered an intrinsic material property. Furthermore, the loss tangent typically peaks in the vicinity of phase transitions and is thus a good indicator of state changes such as the glass or melting transition.[30,40] AFM loss tangent imaging versus temperature can therefore provide valuable information for understanding advanced materials with nanoscale viscoelastic heterogeneity.

We performed temperature-dependent measurements of AFM loss tangent on a polymer film containing a blend of polystyrene (PS) and syndiotactic polypropylene (PP) spin-coated on silicon. The blend contained a continuous PP phase with PS domains. For reference, bulk PS melts at $\sim$240 °C, and syndiotactic PP melts between $\sim$130 °C and 170 °C. A cantilever (Arrow UHFAuD, Nanoworld, Neuchâtel, Switzerland) with a free frequency $f_{\text{free}} = 810\,\text{kHz}$ was excited with photothermal actuation (blueDrive[TM], Asylum Research Oxford Instruments). A commercial AFM instrument with an environmental chamber (Cypher ES, Asylum Research Oxford Instruments) was used to heat and cool the sample with a ramp rate of 0.01 °C/s. With a scan rate of $\sim$9.8 lines per second, each $1024 \times 512$ image took less than 1 min ($\sim$52 s) to acquire.

Figure 1 shows the AFM loss tangent images acquired at several different temperatures as the temperature was ramped from 55 °C to 135 °C and then cooled back to 55 °C. Initially, the images show little contrast between PP and PS. As the temperature is increased, the contrast increases, mainly due to
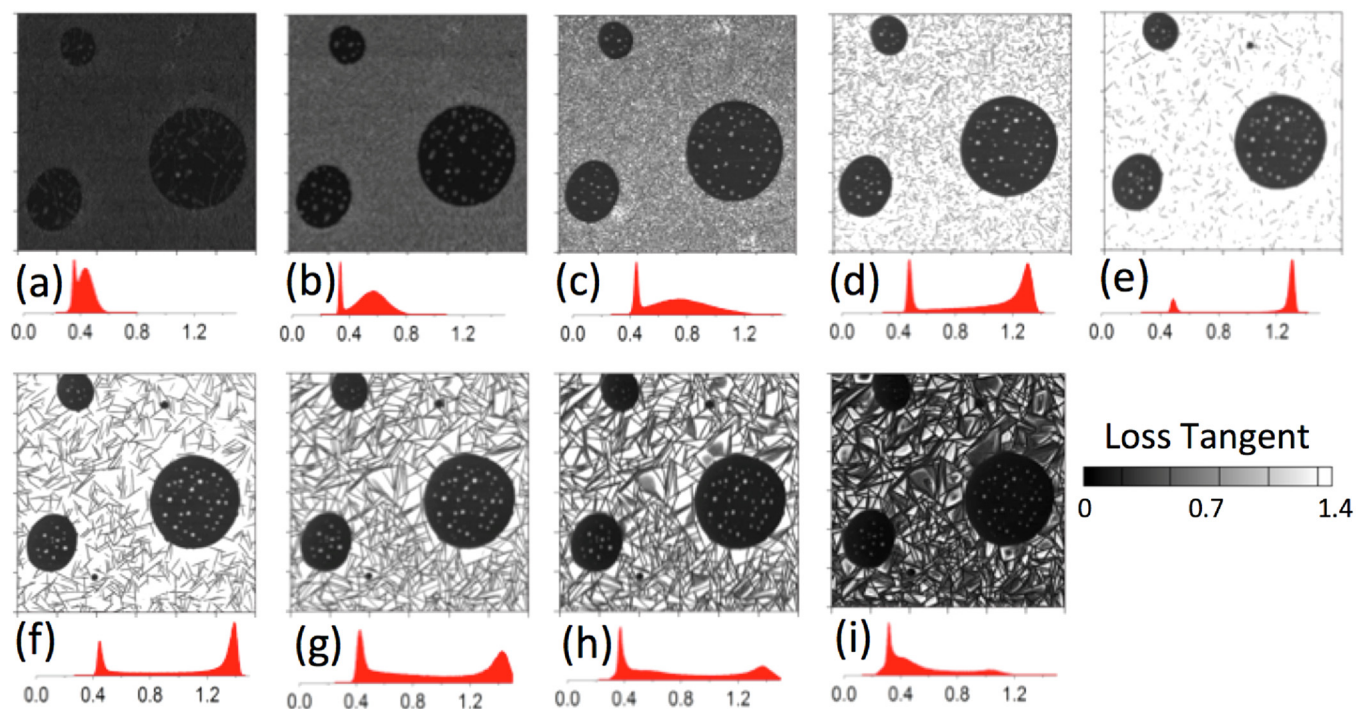


FIG. 1. AFM loss tangent imaging experiments on a polymer film with a continuous phase of PP surrounding PS domains. The loss tangent images were acquired as the film was first heated to (a) 55 °C, (b) 80 °C, (c) 100 °C, (d) 120 °C, and (e) 135 °C, and then cooled to (f) 120 °C, (g) 100 °C, (h) 80 °C, and (i) 55 °C. Scan size 3 $\mu$m.

greater PP loss tangent values. The histograms of each image confirm this behavior and show the relative width of the PP and PS distributions. It can also be seen that while the heating and initial cooling images contain a bimodal distribution, the cooling curves show a trimodal distribution.

The temperature dependence of the AFM loss tangent images is further understood by Fig. 2, which shows the peak values of the PP and PS distributions in the image histograms. The two materials show very different behaviors as the temperature is ramped from 55 °C to 135 °C. The AFM loss tangent values for PS remain relatively constant over the temperature sweep. In fact, there is little or no indication of the glass transition peak typically observed in dynamic mechanical analysis (DMA) measurements at low frequencies (∼0.1–100 Hz). In DMA measurements, the values of the loss tangent at the peak temperature of ∼100–120 °C are typically about two orders of magnitude larger than those at room temperature. This discrepancy is not yet fully understood. Earlier work with contact resonance AFM attributed a similar discrepancy to the tendency for transition temperature to increase with increasing measurement frequency.[41] Given the large frequency difference between DMA and AFM, even a modest effect might shift the peak beyond the maximum temperature used here (135 °C). Further work is needed to determine if the discrepancy is due to a real effect (differences in frequency, bulk versus surface properties, etc.) or a measurement by-product.

In contrast to the PS results, those for PP increase dramatically with increasing temperature. A bifurcation is observed in the PP values during the cooling part of the curve due to formation of amorphous and crystalline phases. As the sample is cooled back to its original temperature, the loss tangent of the crystalline PP regions returns to its original value.

However, the cooled sample now contains additional regions of presumably amorphous PP with much higher loss tangent. One possibility is that these are crystalline regions oriented parallel to the plane of the sample surface, so that amorphous areas are exposed to the cantilever tip.

More generally, Figs. 1 and 2 demonstrate a key advantage of AM-AFM loss tangent imaging. Its ability to provide spatially resolved information on heterogeneous materials is a fundamental improvement on more conventional methods that measure bulk samples. An analogous plot to Fig. 2 for data from a macroscale technique would not contain the spatially resolved information about individual PP regions.

## B. AFM loss tangent imaging of a metallic sample

Viscous damping in metals tends to be much lower than in most polymeric materials. Nevertheless, the viscoelastic loss tangent can exceed 0.1 in metals, especially in softer alloys including lead-tin (Pb-Sn) solder.[42] Viscoelastic effects in these solders can play an important role in device failure modes for electronic components. To perform AFM loss tangent imaging on solder, a sample was prepared by first heating a piece of 50–50 Pb-Sn solder (∼10 mm$^3$) on a hotplate. When the solder reached a molten state, freshly cleaved mica was pressed on top of it. The sample was then promptly removed from the hotplate and, once it had cooled to room temperature, the mica was peeled off to expose a flat solder sample. A nanocrystalline diamond cantilever (ND-DYCRS, Advanced Diamond Technologies Inc., Romeoville, IL) with a spring constant of ∼32 N/m was used in the experiments.

Figure 3(a) shows the surface topography of the solder sample, and Fig. 3(b) shows the corresponding frequency of the cantilever's second resonance measured in AM-FM (amplitude modulated-frequency modulated) mode. Briefly, the second resonance in AM-FM mode is related to the interaction stiffness between the tip and the sample,[43–45] with higher frequency corresponding to higher stiffness. This frequency-shift image clearly resolves different domains on the sample surface, presumably Sn-rich (stiffer) and Pb-rich (softer) domains. Figure 3(c) shows the simultaneously obtained AFM loss tangent image acquired with the cantilever's first resonant mode in AM mode. While there is some crosstalk between the topography and phase channels, this image shows very little contrast correlated with the domains seen in Fig. 3(b). A histogram of the entire AFM loss tangent image in Fig. 3(c) is shown in Fig. 3(e) by the blue bars. To distinguish the loss tangent values in the different material domains, a mask based on the frequency shift image in Fig. 3(b) was constructed. This mask is shown in Fig. 3(d), where red represents the soft domains and green represents the stiff regions. The two different masks were applied to the loss tangent image of Fig. 3(c) to produce the two color-coded histograms in Fig. 3(e). This analysis reveals a small separation between the Pb- and Sn-rich regions.

Although the AFM loss tangent image in Fig. 3 shows the expected contrast, the average value of ∼0.3 is larger than expected. At low frequencies (<10$^{-3}$ Hz), tan δ > 0.1 has been observed in 50–50 Pb-Sn. However, this value decreases as the frequency increases, with tan δ < 4 × 10$^{-3}$
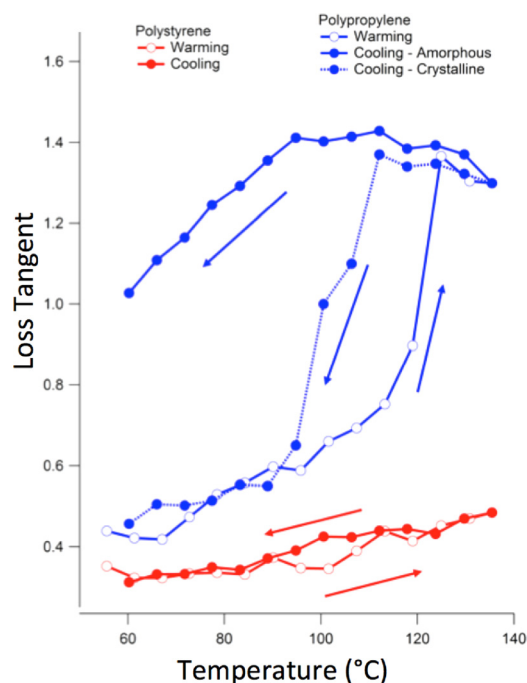
FIG. 2. AFM loss tangent versus temperature for PS (red) and PP (blue) during warming (open symbols) and cooling (closed symbols). The arrows indicate the sequence of measurements. As the film cools, both amorphous (solid line) and crystalline (dotted line) PP phases are formed.
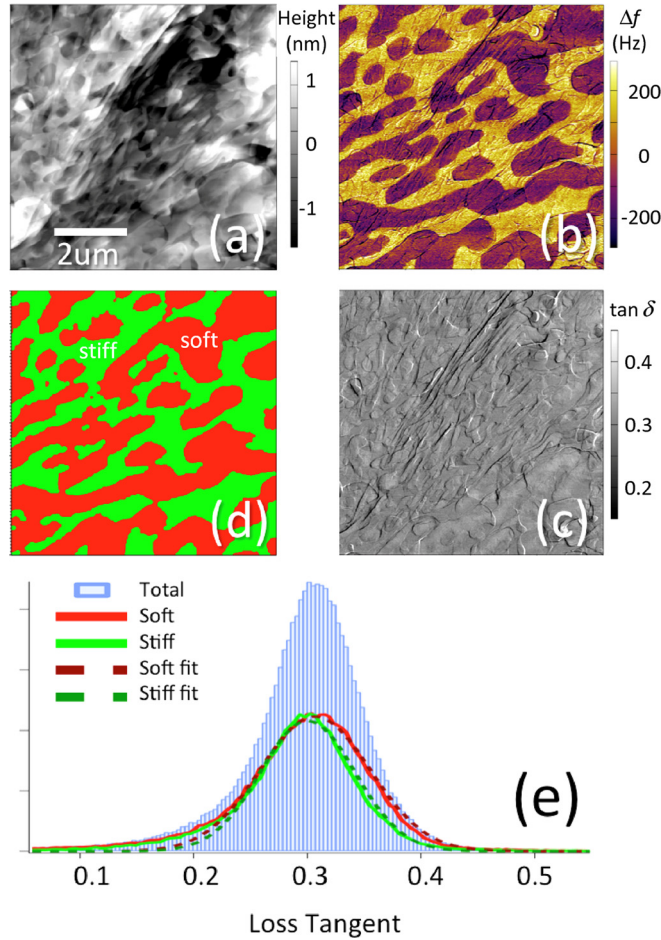
FIG. 3. AFM loss tangent experiments on a two-component solder sample. (a) Topography and (b) AM-FM mode frequency shift of the second mode resonance, which is proportional to the relative stiffness of the tip-sample interaction. The stiffness image shows bright Sn-rich and dark Pb-rich regions. (c) Corresponding AFM loss tangent image with essentially no contrast between the two regions. (d) A binary stiffness map created from (b) that was used to mask the loss tangent image in (c) and produce the two color coded histograms in (e).

at $10^5$ Hz,[46] the approximate range of the tapping frequency for the measurements described here.

## IV. QUANTIFYING THE AFM LOSS TANGENT

In the rest of this paper, we explore error sources and limits on AM-AFM loss tangent measurements. In part, this was motivated by a common feature of the data shown in Figs. 1–3: while the relative contrast between materials was consistent with expectations, the absolute values were systematically larger than expected. Specifically, we will explore the issues listed below.

(1) Random errors—Thermal and other sorts of random errors will set a minimum detectable threshold for the

AFM loss tangent, typically in the range of $10^{-2}$. This random noise is typically dominated by Brownian motion of the cantilever for our microscope in AM mode. If other detector noise such as shot noise becomes significant, it must be included as well.

(2) Systematic errors—These are mostly associated with choosing the appropriate reference point for zero dissipation. We have found it convenient to divide this into two considerations:

   (a) Correctly defining the cantilever reference parameters. These include the resonance frequency, the quality factor, the free amplitude, and the phase offset that describes ubiquitous instrumental phase shifts.

   (b) Measuring the cantilever free amplitude and resonant frequency at every pixel with use of a novel interleaved scanning technique.

(3) Model deviations—The presence of forces other than linear viscoelastic interactions between the tip and the sample.

To begin the discussion of noise, it is useful to map the observables amplitude and phase onto the AFM loss tangent. Figure 4(a) shows a contour plots of tan $\delta$ versus phase $\phi$ and relative amplitude $\alpha$ created with Eq. (2). In this figure, tan $\delta$ is constant along a particular contour, even though the amplitude and phase values continuously vary. The lower boundary (black dotted line) in Fig. 4(a) represents the case of zero dissipation, where the interaction between the tip and the sample is perfectly elastic. This curve is given by the zero-dissipation expression $\sin \phi = A/A_{\text{free}}$ from Ref. 25. The phase values near this boundary are to be expected when measuring relatively loss-free metals, ceramics, and other materials with low losses and high modulus. Any experimental phase and amplitude values below this boundary represent a violation of energy conservation and presumably indicate improper calibration of the cantilever parameters.

Above the no-loss boundary in Fig. 4(a), the colored lines represent the contours of constant loss tangent. At an amplitude ratio $\alpha$, increasing phase $\phi$ corresponds to increasing loss tangent. As the value of tan $\delta$ increases, the contours approach the upper boundary of $\phi = 90°$. This corresponds to the case of all dissipation with no elastic storage, such as expected for a purely viscous fluid. The remainder of Fig. 4, showing the signal-to-noise ratio (SNR) for various amounts of systematic and random noise on the observables, is discussed in Sec. V.

## V. MEASUREMENT UNCERTAINTY

With standard error analysis, the random uncertainty in AFM loss tangent imaging $\Delta_r(\tan \delta)$ associated with uncorrelated random uncertainty $\Delta_r\phi$, $\Delta_r\Omega$, $\Delta_r\alpha$, and $\Delta_rQ$ in $\phi$, $\Omega$, $\alpha$, and $Q$, respectively, is given by

$$\Delta_r(\tan \delta) = \sqrt{\left[\frac{\partial(\tan \delta)}{\partial \phi}\right]^2 (\Delta_r\phi)^2 + \left[\frac{\partial(\tan \delta)}{\partial \Omega}\right]^2 (\Delta_r\Omega)^2 + \left[\frac{\partial(\tan \delta)}{\partial \alpha}\right]^2 (\Delta_r\alpha)^2 + \left[\frac{\partial(\tan \delta)}{\partial Q}\right]^2 (\Delta_rQ)^2}. \tag{3}$$
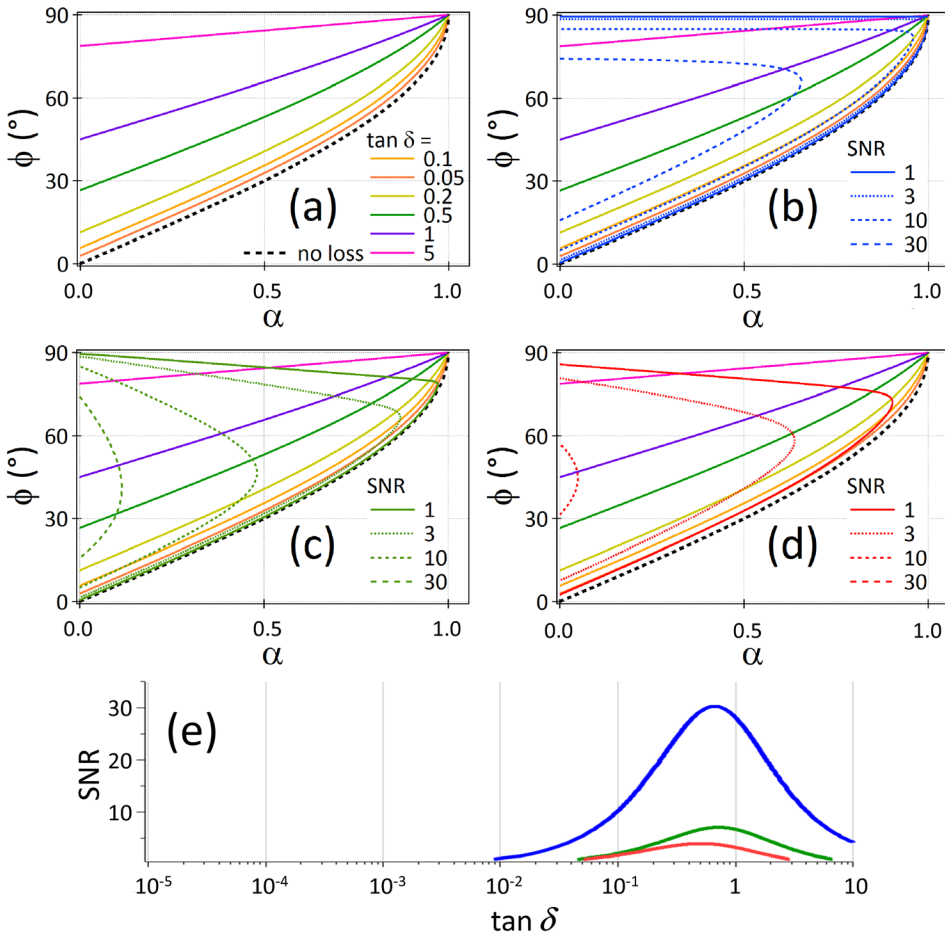
FIG. 4. (a) AFM loss tangent contours as a function of cantilever setpoint amplitude α and phase φ for operation on resonance ($\Omega = 1$). For reference, the dashed black line shows the zero loss case, that is, $\tan \delta = 0$, for a lossless, perfectly elastic material. Similarly, the line at $\phi = 90°$ represents the case for a perfectly lossy material with no elastic component (for example, a viscous liquid). (b)–(d) Contours of constant signal-to-noise ratio (SNR) determined with different uncertainty combinations, as shown in Table I and discussed in the text. (e) SNR curves calculated from the error conditions listed in Table I and extracted from the data in (b) (blue), (c) (green), and (d) (red) at a 50% setpoint ratio ($\alpha = 0.5$).

Similarly, the systematic uncertainty in AFM loss tangent imaging $\Delta_s(\tan \delta)$ due to systematic uncertainty $\Delta_s\phi$, $\Delta_s\Omega$, $\Delta_s\alpha$, and $\Delta_s Q$ is given for small uncertainty values by

$$\Delta_s(\tan \delta) = \frac{\partial(\tan \delta)}{\partial \phi} \Delta_s\phi + \frac{\partial(\tan \delta)}{\partial \Omega} \Delta_s\Omega$$
$$+ \frac{\partial(\tan \delta)}{\partial \alpha} \Delta_s\alpha + \frac{\partial(\tan \delta)}{\partial Q} \Delta_s Q. \quad (4)$$

For the case of both systematic and random uncertainty, the total uncertainty is determined by

$$\Delta_{tot}(\tan \delta) = \sqrt{[\Delta_s(\tan \delta)]^2 + [\Delta_r(\tan \delta)]^2}. \quad (5)$$

The separate derivatives in the above two equations for random and systematic uncertainty can be evaluated as

$$\frac{\partial(\tan \delta)}{\partial \phi} = \frac{1 + \alpha Q(\Omega^2 - 1)\cos \phi - \alpha\Omega \sin \phi}{[\alpha Q(\Omega^2 - 1) + \cos \phi]^2}, \quad (6)$$

$$\frac{\partial(\tan \delta)}{\partial \alpha} = -\frac{\Omega\cos\phi + Q(\Omega^2 - 1)\sin \phi}{[\alpha Q(\Omega^2 - 1) + \cos \phi]^2}, \quad (7)$$

$$\frac{\partial(\tan \delta)}{\partial \Omega} = \frac{\alpha Q[\alpha(\Omega^2 + 1) - 2\Omega \sin \phi] - \alpha \cos \phi}{[\alpha Q(\Omega^2 - 1) + \cos \phi]^2}, \quad (8)$$

and

$$\frac{\partial(\tan \delta)}{\partial Q} = \frac{\alpha(\Omega^2 - 1)(\alpha\Omega - \sin \phi)}{[\alpha Q(\Omega^2 - 1) + \cos \phi]^2}. \quad (9)$$

As a specific example comparing the relative weights of the foregoing terms, we assume a cantilever similar to those used in the experiments discussed below, the AC240 from Olympus, with the following operating parameters: $\Omega = 1$, $\alpha = 0.5$, $Q = 150$, and $\alpha = A/A_{\text{free}}$. These conditions correspond to operating on resonance with a setpoint ratio of 0.5 (i.e., AM mode amplitude is 50% of the free amplitude). The value $\tan \delta = 0.1$ is assumed, as expected for a polymer such as high-density polyethylene. From Eq. (1), these values yield a cantilever phase shift $\phi \approx 36°$ (refer to Fig. 4(a) to see this graphically). With Eqs. (6)–(9), the individual error terms can be evaluated as $\frac{\partial(\tan \delta)}{\partial \phi} = 0.019/°$, $\frac{\partial(\tan \delta)}{\partial \alpha} = -1.24$, $\frac{\partial(\tan \delta)}{\partial \Omega} = -20.7$, and $\frac{\partial(\tan \delta)}{\partial Q} = 0$. In terms of systematic error, typical values of uncertainty in amplitude, phase, and tuning frequency are $\Delta_s\phi = 0.3°$, $\Delta_s\alpha = 10^{-2}$, and $\Delta_s\Omega = 10^{-3}$, respectively, for the first mode in our experience.

These values yield a combined systematic error estimate $\Delta_s(\tan \delta) = 0.026$. This result is surprisingly large, given that the viscoelastic loss tangent of many polymer materials is of similar order or smaller. Of the three contributions, the largest is from the uncertainty in tuning frequency $\Delta_s\Omega$. If

that is improved to $\Delta_s \Omega = 10^{-4}$, the AFM loss tangent uncertainty is reduced to $\Delta_s(\tan\delta) = 0.016$. This result implies that careful identification of the cantilever resonance frequency is important for quantitative estimation. While this level of tuning uncertainty is not typical for AM-mode operation, it is achievable. An informal survey of automatic tuning functions on a variety of commercial AFM instruments yielded scatter as large as 1 kHz and typically on the order of several hundred hertz in the identification of the resonant frequency. In the course of the investigations discussed here, we have improved our tuning routine to bring the frequency uncertainty closer to a few tens of hertz, $\Delta_s\Omega \leq 10^{-4}$, without adding significant time to the procedure.

It is also useful to define the SNR to consider how it affects the AFM loss tangent measurement

$$SNR = \frac{\tan\delta}{\Delta(\tan\delta)}. \tag{10}$$

Typically, we would like $SNR \geq 1$ so that the signal is larger than the uncertainty. For the example above with the AC240 Olympus cantilever and $\tan\delta = 0.1$, this corresponds to tuning the cantilever to within $\sim$300–400 Hz of the 75 kHz resonance. To better visualize the interdependence of the SNR on the parameters discussed above, Figs. 4(b)–4(d) show the curves of constant SNR as a function of relative amplitude $\alpha$ and phase $\phi$. The SNR curves were determined by finding the values of $\alpha$ and $\phi$ that simultaneously satisfy Eqs. (2) and (10) for a given value of SNR. The values in Table I below for different elements of measurement uncertainty were used in Eqs. (3)–(5) to obtain the overall uncertainty $\Delta_{tot}(\tan\delta)$ needed in Eq. (10). For this purpose, it is assumed that the random phase error is dominated by thermal motion with $\Delta_r\phi = 0.5°$. The overall uncertainty increases from the thermal-noise-limited case in Fig. 4(a) to a case with both random and systematic errors in Fig. 4(d). As the uncertainty increases, the accessible region of $(\alpha, \phi)$ space for a given SNR decreases significantly. The highest errors occur at the boundaries of the physically meaningful phase and amplitude values. Near the no-loss boundary, the uncertainty contributions are larger than the loss tangent value itself, as discussed above. For large loss tangent values, note that the tangent function diverges at 90°. Thus, small errors in phase or amplitude can lead to enormous errors in the estimated loss tangent.

Figure 4(e) shows the SNR curves from the error conditions listed in Table I and extracted from the data of Figs. 4(b) (blue), 4(c) (green), and 4(d) (red) at a 50% setpoint ratio ($\alpha = 0.5$). As noted in Table I, the blue curve

shows the minimum-noise case limited by the fundamental thermal physics of the cantilever, while the green and red curves show the effects of increasing random and systematic noise. It is clear from the blue curve in Fig. 4(e) that even in the most optimistic experimental case of the blue curve, thermal noise still limits loss tangent measurements to approximately $0.01 < \tan\delta < 5$.

Figure 5 puts these SNR concepts into context for actual materials. Figure 5(a) is a replotting of the SNR versus loss tangent of Fig. 5(e), where we have swapped the vertical and horizontal axes. The colored windows in Figure 5 correspond to regions with $SNR > 1$ and are color-coded to the curves in Fig. 4(e). Regions with $SNR < 1$ are indicated by the gray window. As discussed for Fig. 4(e), even the most optimistic error estimate indicated by the blue window—limited only by the fundamental limit of cantilever thermal noise—still rules out measurements for $\tan\delta < 0.01$. Figure 5(b) shows the viscoelastic loss tangent versus elastic modulus for a large range of materials, adapted from Ref. 42. Note there is a general trend that materials with lower elastic modulus tend to also have a proportionally higher viscoelastic loss tangent. The room temperature loss tangent and modulus of the materials imaged in Fig. 1 (3) are indicated by the blue (red) circles. The polymers of Fig. 1 are well separated and above the threshold of 0.01, consistent with the high SNR values evident in Fig. 1.

From a historical perspective, it is interesting that Fig. 5 is remarkably consistent with the phase imaging literature. While there are a plethora of examples of phase imaging of polymers and rubbers (all typically with $\tan\delta \gtrsim 0.01$), there are extremely few examples of phase contrast over higher modulus materials where we would expect $\tan\delta < 0.01$.

## VI. OTHER CONTRIBUTIONS TO AFM LOSS TANGENT

As mentioned above, a number of conservative and dissipative interactions contribute to AFM loss tangent estimation in addition to the linear viscoelastic interactions between the tip and the sample. In fact, depending on the experimental parameters and settings, the sample loss and storage moduli may contribute only a small portion of the signal in the loss tangent estimation. It is up to the experimentalist to operate the cantilever so that the AFM instrument measures the loss tangent of interest. For example, when imaging the mechanical loss tangent of a polymer surface, it is important to operate in repulsive mode, so that the cantilever interacts with the short-range repulsive forces controlled by the sample's viscoelastic properties. In this section, we consider some of these contributions, including experimental factors such as air damping and surface hydration layers, and material effects such as viscoelastic nonlinearity.

### A. Air damping effects

Proper choice of the zero-dissipation point is critical for proper calibration of the tip-sample dissipation. In particular, squeeze film damping[47,48] can have a strong effect on the measured dissipation. Squeeze film damping causes the cantilever damping to increase as the body of the cantilever moves closer to the sample surface. For rough or uneven surfaces, this can mean that the cantilever body height changes with respect to the average sample position enough

TABLE I. Error parameters for Figs. 4(b)–4(d). The values are used in each image of Fig. 4 for the random (subscript $r$) and systematic (subscript $s$) errors in relative frequency $\Delta\Omega$ and phase $\Delta\phi$. Other error sources are held constant as follows: $\Delta\alpha_r = \Delta\alpha_s = 0$ and $\Delta Q_r = \Delta Q_s = 0$.

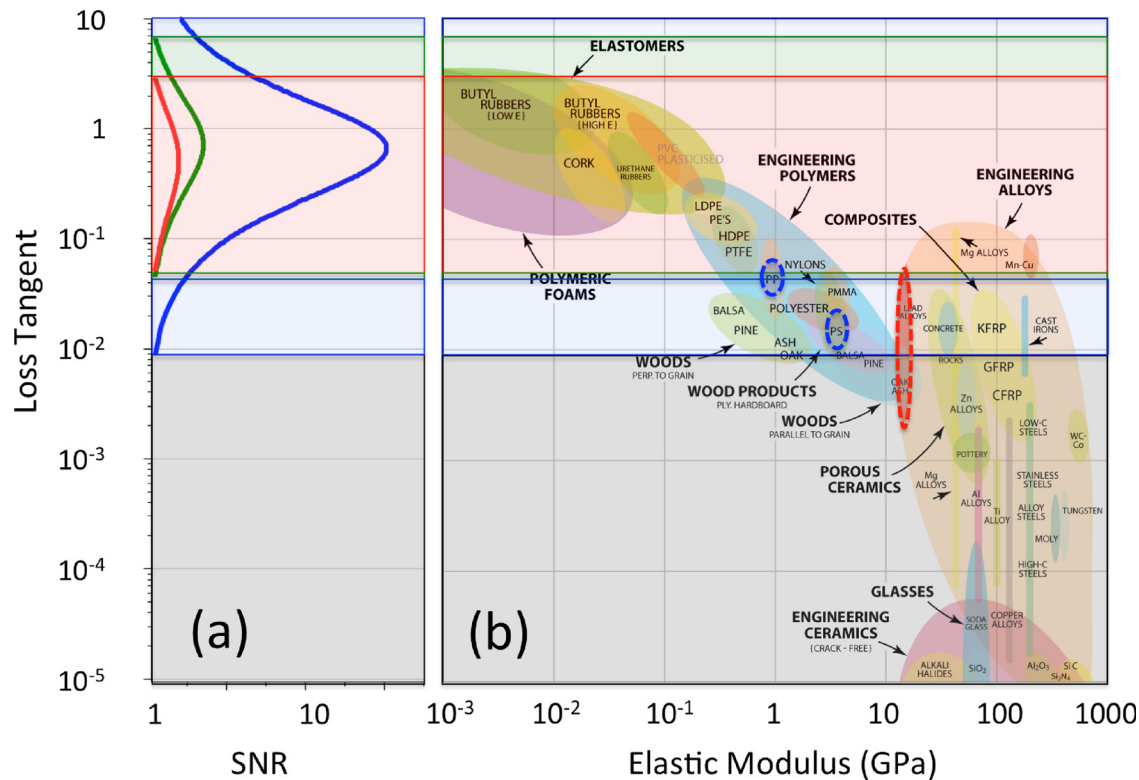| Figure and color | $\Delta\Omega_r$ | $\Delta\Omega_s$ | $\Delta\varphi_r(°)$ | $\Delta\varphi_s(°)$ |
|---|---|---|---|---|
| 4(a) | 0 | 0 | 0 | 0 |
| 4(b), blue | 0 | 0 | 0.5 | 0 |
| 4(c), green | $10^{-5}$ | $10^{-4}$ | 0.5 | 0 |
| 4(d), red | $10^{-5}$ | $10^{-4}$ | 0.5 | 2 |

FIG. 5. (a) Error contours that show the achievable signal to noise ratio in the measured AFM loss tangent for the different error estimates given in Table I. (b) Viscoelastic loss tangent versus elastic modulus for common materials, adapted from Ref. 42. The polymers present in the sample of Fig. 1 are circled in blue, while the solder alloy in the sample of Fig. 3 is circled in red.

to cause crosstalk artifacts in the measured dissipation and therefore the measured AFM loss tangent.

An example of air damping effects is shown in Fig. 6. The sample was a silicon (Si) wafer patterned with a film of SU-8, an epoxy resin commonly used for photolithography. The elastic modulus of silicon is relatively high (∼150–160 GPa), and the viscoelastic loss tangent is very low (∼$10^{-6}$).[49] Because SU-8 is a highly crosslinked polymer with a glass transition temperature much higher than room temperature (>200 °C), its elastic modulus is ∼2–4 GPa (Ref. 50), and its loss tangent is ∼0.01–0.05 at room temperature.[51] A cantilever of the type described above (Olympus AC240) was used to acquire topography and loss tangent images. As the topography image in

Fig. 6(a) shows, the SU-8 film was approximately 1.5 μm thick.

The AFM loss tangent image in Fig. 6(c) has a large overall value of ∼0.3. Perhaps more troubling is that the AFM loss tangent measured on the Si sample is larger than that measured on the SU-8: $\tan\delta(\text{Si}) > \tan\delta(\text{SU-8})$. As we will show below, both of these issues are mitigated by considering another source of energy dissipation: air squeeze film damping. Because the Si substrate is ∼1.5 μm lower than the SU-8 film, the cantilever body is much closer to the sample when the tip is measuring the Si. The cantilever therefore experiences greatly increased air damping, which is interpreted as larger AFM loss tangent. In general, the magnitude of this
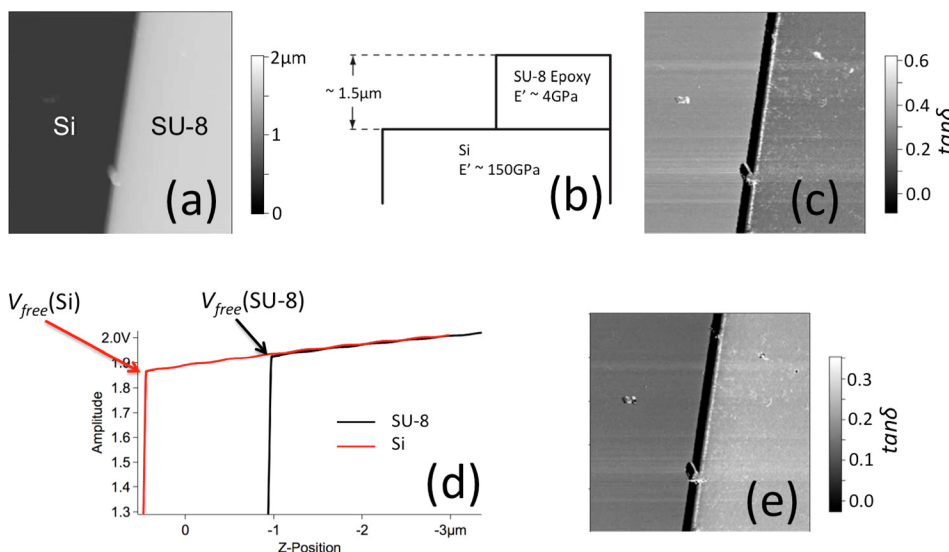


FIG. 6. Squeeze film damping effects in AFM loss tangent imaging. (a) Topography image of a Si wafer with a patterned film of SU-8 epoxy and (b) sample schematic in cross section. (c) The corresponding AFM loss tangent image surprisingly indicates that the cantilever loss tangent is higher over the Si wafer than over the relatively lossy SU-8 polymer. (d) Dynamic force curve measuring oscillation amplitude as a function of z-piezo position over Si (red) and SU-8 (black). (e) Corrected image acquired by the procedure described in the text, which recovers the expected relative contrast in loss tangent.

effect and its variation with $(x,y)$ position depend on sample geometry and cantilever orientation. Figure 6(d) shows that the reference free air amplitudes for the cantilever are different over the two regions, presumably due to the large difference in height between the two materials. As mentioned above, these reference values are critical for correctly calculating the AFM loss tangent.

## B. Two-pass imaging to correct for air damping

To correct for air damping effects in AFM loss tangent measurements, we use the two-pass imaging technique described schematically in Fig. 7. The first pass is the normal AM imaging pass, indicated in blue in Fig. 7(a). This pass operates as in conventional AM imaging, and the amplitude $V$ (or equivalently $A$) and the phase $\phi$ are measured at each $(x,y)$ pixel, while the cantilever taps the surface. The second pass is a reference calibration pass, or "nap pass," shown in red in Fig. 7(a). (The term "nap pass" derives from the aviation expression "nap-of-the-earth flight," in which a plane makes a contour-hugging flight at low altitude.) In the nap pass, the cantilever is scanned at a preset relative height $\Delta z$ above the surface. In principle, $\Delta z$ should be as small as possible for accurate calibration. However, experimentally it may be difficult to scan at extremely low heights, and typically $\Delta z \approx$
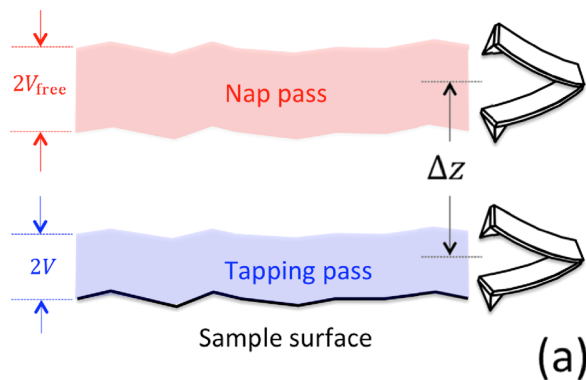


FIG. 7. Concepts of two-pass technique for AFM loss tangent imaging. (a) The normal amplitude modulation (AM) imaging pass is indicated in blue, and the phase-locked loop (PLL) reference calibration pass is shown in red. The reference position at each $(x, y)$ pixel location is set by the relative height $\Delta z$. (b) The variables in the equation for AFM loss tangent $\tan \delta$ color coded to the appropriate steps in the calibration procedure: the initial cantilever tune (green); the first, conventional AM pass (blue); and the second, nap pass (red).

50–100 nm in practice. The cantilever is operated during the nap pass in a phase-locked loop (PLL) that keeps it at reference. During the nap pass, the free reference values of the frequency $\omega_{\text{free}}$ and the amplitude $V_{\text{free}}$ or $A_{\text{free}}$ are measured at each $(x,y)$ pixel. The color-coded AFM loss tangent equation in Fig. 7(b) explains how the two-pass procedure enables a corrected calibration on a pixel-by-pixel basis. In addition to the information obtained in two-pass imaging, the cantilever drive frequency $\omega$ and quality factor $Q$ (green in Fig. 7(b)) are needed. These are measured in a separate cantilever tune that is usually performed prior to imaging.

To demonstrate the two-pass imaging technique, we applied it to the Si/SU-8 sample described above. Figure 6(e) shows the resulting AFM loss tangent image corrected for air damping effects. Unlike the single-pass results in Fig. 6(c), the values in Fig. 6(e) display the expected contrast, namely, $\tan \delta(\text{Si}) < \tan \delta(\text{SU-8})$.

## C. Capillary effects

Although the two-pass correction approach recovers the correct viscoelastic contrast trend, the overall average loss tangent in Fig. 6(e) is still larger than expected for a Si or SiO$_2$ surface, with $\tan \delta(\text{Si}) \approx 0.1$. In addition to the squeeze film damping issues discussed above, this may originate from other sources of surface damping, specifically the hydration layer. This layer of adsorbed water can form on both the sample and the tip under ambient conditions and depends on relative humidity and surface chemistry. As a result, a capillary bridge is formed and ruptured during each AM mode oscillation cycle, providing another source of energy dissipation.[52,53] Like the other dissipative terms discussed here, the effect of the water layer is to increase the numerator in Eq. (1) and thus increase the overall value of AFM loss tangent. The magnitude of this
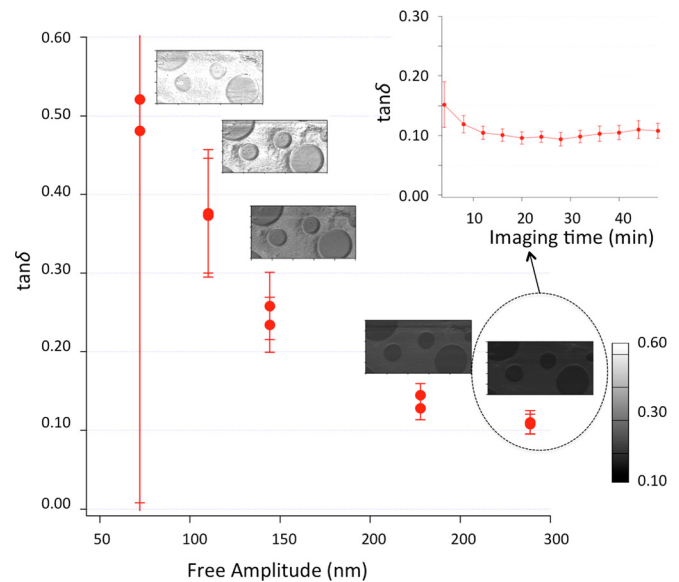


FIG. 8. Measured AFM loss tangent versus cantilever free amplitude $A_{\text{free}}$ for a PS-PP film with the AM setpoint maintained at $A_{\text{free}}/2$ ($\alpha = 0.5$). The inset images measured at each amplitude value are scaled the same as shown by the color bar. The inset graph shows a typical time evolution of the loss tangent measurement for the largest value of $A_{\text{free}}$. After the first image, the estimation remains relatively constant.

effect depends on a complex interplay of cantilever and water layer parameters including tip radius, oscillation amplitude, and surface energy. As such, it is not straightforward to quantify the impact on loss tangent estimates, and further investigation through both modeling and experiments is needed.

The experiments in Fig. 8 are a first step in understanding these issues. The figure shows how the AFM loss tangent estimate improves with cantilever oscillation amplitude on a spin-coated film of PP and PS. In the imaging experiments, the free amplitude $A_{\text{free}}$ was varied, while the setpoint ratio $\alpha = A/A_{\text{free}}$ was held constant at 0.5. For each value of $A_{\text{free}}$, two points are plotted that represent the average values of $\tan\delta$ in the PP and PS regions of the corresponding inset images. It can be seen that as $A_{\text{free}}$ increases from 70 nm to 290 nm, the estimations of $\tan\delta$ decrease and approach the range of values expected for PS ($\sim$0.01–0.03) and PP($\sim$0.04–0.07). As the free amplitude increases, the tip spends more time interacting with the viscoelastic contact forces. Thus, the relative contribution of these forces to the AFM loss tangent increases, and the AFM loss tangent estimate approaches the ideal limit. In addition, the measurement uncertainty (indicated by the error bars of one standard deviation) decreases dramatically.

## D. Material effects: Nonlinear viscoelasticity and plasticity

Finally, we briefly discuss two aspects of material behavior that affect AFM loss tangent estimates. The first concerns the material's viscoelastic response. Implicit in our definition and use of the AFM loss tangent expression is the assumption that the sample measured with the indenting AFM tip can be described as a linear viscoelastic material. In this limit, the strains remain small and follow a linear stress-strain relationship, so that an increase in stress increases the strain by the same factor. However, the assumption of linear viscoelasticity may not always hold. For instance, the chosen experimental settings may apply sufficiently large stresses to cause a non-linear material response. In such cases, AFM loss tangent measurements will not accurately represent the viscoelastic $\tan\delta$ of the material. One test for nonlinear response or improper experimental parameters is to measure the AFM loss tangent as a function of indentation depth, because it should not exhibit a depth dependence.[40]

Another consideration is the potential for plastic deformation of the sample (or tip, in the case of hard samples). As the extreme limit of nonlinear viscoelasticity, plastic deformation of the sample represents irreversible work that will appear in the numerator of the loss tangent estimation. Any plastic work done by the tip on the surface, even if only in the first tap, will be indistinguishable from sample dissipation (i.e., $G''$) and should thus contribute to an overestimation of the AFM loss tangent. The complex theory of indentation-induced plasticity in materials is strongly dependent on indenter shape and is beyond the scope of this work.[54,55] However, we can estimate the yield stress $Y$ from its relation to the force $F_{\text{plastic}}$ needed for plastic deformation[55]

$$F_{\text{plastic}} = \frac{(16\pi)^2}{6}\left(\frac{R}{E_c}\right)^2 Y^3, \tag{11}$$

where $R$ is the radius of curvature of the hemispherical indenter tip. $E_c$ is the reduced or effective modulus defined by $\frac{1}{E_c} = \frac{1-\nu_t^2}{E_t} + \frac{1-\nu_s^2}{E_s}$, where $E$ and $\nu$ are Young's modulus and Poisson's ratio, respectively, and the subscripts $t$ and $s$ indicate the tip and sample, respectively. Approximate guidelines for yield stress values in common materials are $\sim$10 MPa for elastomers (butyl rubbers, polyurethane, etc.), 50–100 MPa for engineering polymers (polystyrene, polypropylene, etc.), 100–500 MPa for metallic alloys (Cu, Ni, Ti, etc.) and $>$1 GPa for engineering ceramics ($Al_2O_3$, $Si_3N_4$, etc.).[42]

We can use Eq. (11) to explore the relationship between Young's modulus and strength for a range of common materials. Here, the term "strength" corresponds to yield strength for metals and polymers, compressive crushing strength for ceramics, tear strength for elastomers and tensile strength for composites and woods.[42] With $R = 10$ nm and $F_{\text{plastic}} = 1$ pN, 1 nN, and 1 $\mu$N in Eq. (11), we find that a significant fraction of materials are expected to plastically yield for loading forces between 1 and 10 nN, a range typical in AM-AFM experiments. This illustrates the importance of using the appropriate operating forces when performing experiments.

Furthermore, plastic deformation can lead to the formation of surface debris, which may also result in contamination of the AFM tip. In this case, dissipation at the debris-sample and debris-tip interfaces may provide additional contributions to the AFM loss tangent measurement. It is therefore important to understand and minimize contaminants on the surface.

## VII. CONCLUSION

Creating a reliable experimental technique from a theoretical concept requires careful evaluation of many measurement issues. Here, we have considered several practical factors for implementing AFM loss tangent imaging in AM mode. By itself, phase contrast in AM mode is useful for differentiating materials and resolving fine structural features. However, by combining the phase and amplitude signals, the AFM loss tangent interpretation of AM mode allows us to view phase imaging in a new light and improves its outlook for reliable, quantitative nanomechanical characterization. Because it describes the entire cantilever and tip-sample interaction, the AFM loss tangent expression provides an upper limit to the actual viscoelastic loss tangent of the sample. It avoids error from absolute amplitude measurements, but typical experimental conditions restrict applicability to approximately $\tan\delta \geq 0.01$, even when uncertainty is limited only by thermal noise. Error due to air damping effects can be corrected with a novel two-pass imaging approach that calibrates the free air amplitude and frequency. Both conservative interactions such as nonlinear viscoelasticity and dissipative interactions such as chemical adhesion and plasticity serve to increase the measured AFM loss tangent value. Our results provide deeper insight into loss tangent methods and show progress toward the goal of accurate nanomechanical imaging with AFM.

[1]G. Binning, C. F. Quate, and C. Gerber, "Atomic force microscope," Phys. Rev. Lett. **56**, 930 (1986).

[2]Y. Martin, C. C. Williams, and H. K. Wickramasinghe, "Atomic force microscope–force mapping and profiling on a sub 100-Å scale," J. Appl. Phys. **61**, 4723 (1987).

[3]R. Garcia, *Amplitude Modulation Atomic Force Microscopy* (Wiley-VCH, Weinheim, 2010).

[4]M. F. Finlan and I. A. McKay, U.S. patent No. 5,047,633 (3 May 1990).

[5]G. M. McClelland, R. Erlandsson, and S. Chiang, "Atomic force microscopy: General principles and a new implementation," in *Review of Progress in Quantitative Nondestructive Evaluation 7B* (Plenum, New York, 1987), pp. 1307–1314.

[6]P. Gleyzes, P. K. Kuo, and A. C. Boccara, "Bistable behavior of a vibrating tip near a solid-surface," Appl. Phys. Lett. **58**, 2989 (1991).

[7]V. B. Elings and J. Gurley, U.S. patent No. 5,412,980 (7 August 1992).

[8]Q. Zhong, D. Inniss, K. Kjoller, and V. B. Elings, "Fractured polymer/silica surface studied by tapping mode atomic force microscopy," Surf. Sci. Lett. **290**, L688 (1993).

[9]D. A. Chernoff, "High resolution chemical mapping using tapping mode AFM with phase contrast," in *Proceedings of Microscopy and Microanalysis*, edited by G. W. Bailey, M. H. Ellisman, R. A. Henniger, and N. J. Zaluzec (Jones and Begell, New York, 1995), pp. 888–889.

[10]P. Achalla, J. McCormick, T. Hodge, C. Moreland, P. Esnault, A. Karim, and D. Raghavan, "Characterization of elastomeric blends by atomic force microscopy," J. Polym. Sci., Part B **44**, 492 (2006).

[11]D. Wang, S. Fujinami, K. Nakajima, S. Inukai, H. Ueki, A. Magario, T. Noguchi, M. Endo, and T. Nishi, "Visualization of nanomechanical mapping on polymer nanocomposites by AFM force measurement," Polymer **51**, 2455 (2010).

[12]S. M. Gheno, F. R. Passador, and L. A. Pessan, "Investigation of the phase morphology of dynamically vulcanized PVC/NBR blends using atomic force microscopy," J. Appl. Polym. Sci. **117**, 3211 (2010).

[13]M. Qu, F. Deng, S. M. Kalkhoran, A. Gouldstone, A. Robisson, and K. J. Van Vliet, "Nanoscale visualization and multiscale mechanical implications of bound rubber interphases in rubber-carbon black nanocomposites," Soft Matter **7**, 1066 (2011).

[14]J. K. Hobbs, O. E. Farrance, and L. Kailas, "How atomic force microscopy has contributed to our understanding of polymer crystallization," Polymer **50**, 4281 (2009).

[15]J. H. Park, Y. Sun, Y. E. Goldman, and R. J. Composto, "Amphiphilic block copolymer films: Phase transition, stabilization, and nanoscale templates," Macromolecules **42**, 1017 (2009).

[16]A. B. Djurisic, H. Wang, W. K. Chan, and M. H. Xie, "Characterization of block copolymers using scanning probe microscopy," J. Scanning Probe Microsc. **1**, 21 (2006).

[17]J. B. Pethica and W. C. Oliver, "Tip surface interactions in STM and AFM," Phys. Scr. **1987**, 61 (1987).

[18]R. Garcia, J. Tamayo, and A. San Paulo, "Phase contrast and surface energy hysteresis in tapping scanning force microscopy," Surf. Interface Anal. **27**, 312 (1999).

[19]Y. Zhao, Q. Cheng, M. Qian, and J. H. Cantrell, "Phase image contrast mechanism in intermittent contact atomic force microscopy," J. Appl. Phys. **108**, 094311 (2010).

[20]W. Xu, P. M. Wood-Adams, and C. G. Robertson, "Measuring local viscoelastic properties of complex materials with tapping mode atomic force microscopy," Polymer **47**, 4798 (2006).

[21]F. Dubourg, J. P. Aime, S. Marsaudon, R. Boisgard, and P. Leclere, "Probing viscosity of a polymer melt at the nanometer scale with an oscillating nanotip," Eur. Phys. J. E **6**, 49 (2001).

[22]G. J. C. Braithwaite and P. F. Luckham, "The simultaneous determination of the forces and viscoelastic properties of adsorbed polymer layers," J. Colloid Interface Sci. **218**, 97 (1999).

[23]A. Noy, C. H. Sanders, D. V. Vezenov, S. S. Wong, and C. M. Lieber, "Chemically sensitive imaging in tapping mode by chemical force microscopy: Relationship between phase lag and adhesion," Langmuir **14**, 1508 (1998).

[24]J. Tamayo and R. Garcia, "Effects of elastic and inelastic interactions on phase contrast images in tapping-mode scanning force microscopy," Appl. Phys. Lett. **71**, 2394 (1997).

[25]J. P. Cleveland, B. Anczykowski, A. E. Schmid, and V. B. Elings, "Energy dissipation in tapping-mode atomic force microscopy," Appl. Phys. Lett. **72**, 2613 (1998).

[26]N. F. Martinez and R. Garcia, "Measuring phase shifts and energy dissipation with amplitude modulation AFM," Nanotechnology **17**, S167 (2006).

[27]C. J. Gomez and R. Garcia, "Determination and simulation of nanoscale energy dissipation processes in amplitude modulation AFM," Ultramicroscopy **110**, 626 (2010).

[28]A. San Paulo and R. Garcia, "Unifying theory of tapping-mode atomic-force microscopy," Phys. Rev. B **66**, 041406(R) (2002).

[29]R. Proksch and D. Yablon, "Loss tangent imaging: Theory and simulations of repulsive-mode tapping atomic force microscopy," Appl. Phys. Lett. **100**, 073106 (2012).

[30]J. D. Ferry, *Viscoelastic Properties of Polymers* (John Wiley and Sons, New York, 1980).

[31]H. K. Nguyen, M. Ito, S. Fujinami, and K. Nakajima, "Viscoelasticity of inhomogeneous polymers characterized by loss tangent measurements using atomic force microscopy," Macromolecules **47**, 7971 (2014).

[32]C. G. Robertson and M. Rackaitis, "Further consideration of viscoelastic two glass transition behavior of nanoparticle-filled polymers," Macromolecules **44**, 1177 (2011).

[33]R. Mohr, K. Kratz, T. Weigel, M. Lucka-Gabor, M. Moneke, and A. Lendlein, "Initiation of shape-memory effect by inductive heating of magnetic nanoparticles in thermoplastic polymers," Proc. Natl. Acad. Sci. U. S. A. **103**, 3540 (2006).

[34]E. Munch, J. M. Pelletier, B. Sixou, and G. Vigier, "Characterization of the drastic increase in molecular mobility of a deformed amorphous polymer," Phys. Rev. Lett. **97**, 207801 (2006).

[35]B. Hopkinson, "A method of measuring the pressure in the deformation of high explosives or by the impact of bullets," Proc. R. Soc. London A **89**, 411 (1914).

[36]P. C. Painter and M. M. Coleman, *Essentials of Polymer Science and Engineering* (DEStech Publications Inc., Lancaster, PA, 2009).

[37]Y. P. Cao, X. Y. Ji, and X. Q. Feng, "Geometry independence of the normalized relaxation functions of viscoelastic materials in indentation," Philos. Mag. **90**, 1639 (2010).

[38]C. A. Tweedie, G. Constantinides, K. E. Lehman, D. J. Brill, G. W. Blackman, and K. J. Van Vliet, "Enhanced stiffness of amorphous polymer surfaces under confinement of localized contact loads," Adv. Mater. **19**, 2540 (2007).

[39]R. Wagner, R. Moon, J. Pratt, G. Shaw, and A. Raman, "Uncertainty quantification in nanomechanical measurements using the atomic force microscope," Nanotechnology **22**, 455703 (2011).

[40]K. P. Menard, *Dynamic Mechanical Analysis: A Practical Introduction* (CRC Press, Boca Raton, FL, 2008).

[41]I. Chakraborty and D. G. Yablon, "Temperature dependent loss tangent measurement of polymers with contact resonance atomic force microscopy," Polymer **55**, 1609 (2014).

[42]M. F. Ashby, "Overview No. 80: On the engineering properties of materials," Acta Metall. **37**, 1273 (1989).

[43]R. Garcia and R. Proksch, "Nanomechanical mapping of soft matter by bimodal force microscopy," Eur. Polym. J. **49**, 1897 (2013).

[44]See http://www.oxford-instruments.com/OxfordInstruments/media/asylum-research/all-pdfs/Fast-Quantitative-AFM-Nanomechanical-Measurements-Using-AM-FM-Viscoelastic-Mapping-Mode.pdf?width=0&height=0&ext=.pdf for additional information.

[45]U.S. patent Nos. 8,555,711, 8,448,501, 8,024,963, 7,958,563, 7,921,466, and 7,603,891.

[46]L. K. Edwards, R. S. Lakes, and W. A. Nixon, "Viscoelastic behavior of 80In15Pb5Ag and 50Sn50Pb alloys: Experiment and modeling," J. Appl. Phys. **87**, 1135 (2000).

[47]C. P. Green and J. E. Sader, "Frequency response of cantilever beams immersed in viscous fluids near a solid surface with applications to the atomic force microscope," J. Appl. Phys. **98**, 114913 (2005).

[48]M. Bao and H. Yang, "Squeeze film air damping in MEMS," Sens. Actuators, A **136**, 3 (2007).

[49]R. Lakes, *Viscoelastic Materials* (Cambridge University Press, Cambridge, 2009).

[50]H. Lorenz, M. Despont, M. Fahrni, N. LaBianca, P. Vettiger, and P. Renaud, "SU-8: A low-cost negative resist for MEMS," J. Micromech. Microeng. **7**, 121 (1997).

[51]S. Schmid and C. Hierold, "Damping mechanisms of single-clamped and prestressed double-clamped resonant polymer microbeams," J. Appl. Phys. **104**, 093516 (2008).

[52]L. Zitzler, S. Herminghaus, and F. Mugele, "Capillary forces in tapping mode atomic force microscopy," Phys. Rev. B **66**, 155436 (2002).

[53]E. Sahagun, P. Garcia-Mochales, G. M. Sacha, and J. J. Saenz, "Energy dissipation due to capillary interactions: Hydrophobicity maps in force microscopy," Phys. Rev. Lett. **98**, 176106 (2007).

[54]K. L. Johnson, *Contact Mechanics* (Cambridge University Press, Cambridge, UK, 1985).

[55]C. M. Mate, *Tribology on the Small Scale* (Oxford University Press, Oxford, UK, 2008).